sustainability

MDPI

Article

Activated Biochar from Pineapple Crown Biomass: A High-Efficiency Adsorbent for Organic Dye Removal

Francisco J. Cano [1,2], Odín Reyes-Vallejo [3,*], Rocío Magdalena Sánchez-Albores [4], Sebastian P. Joseph [5], Abumalé Cruz-Salomón [4], Maritza del Carmen Hernández-Cruz [4], Wilber Montejo-López [4], Mayram González Reyes [4], Rocío del Pilar Serrano Ramirez [4] and Héctor Hiram Torres-Ventura [4]

[1] Institute of Molecules & Materials of Le Mans (IMMM)—UMR CNRS 6283, Le Mans Université, 72000 Le Mans, France; franciscojavier.cano@outlook.es
[2] Programa de Nanociencias y Nanotecnología, CINVESTAV—IPN, Av. IPN 2508 Col. San Pedro Zacatenco, Ciudad de México 07360, Mexico
[3] Sección de Electrónica de Estado Sólido-Ingeniería Eléctrica (SEES), CINVESTAV—IPN, San Pedro Zacatenco, Ciudad de México 07360, Mexico
[4] Escuela de Ciencias Químicas, Universidad Autónoma de Chiapas (UNACH), Ocozocoautla de Espinosa 29140, Mexico; magdalena.sanchez@unach.mx (R.M.S.-A.); abumale.cruz@unach.mx (A.C.-S.); maritza.hernandez@unach.mx (M.d.C.H.-C.); wilber.montejo@unach.mx (W.M.-L.); mayram.gonzalez@unach.mx (M.G.R.); rocio.serrano@unach.mx (R.d.P.S.R.); hector.torres@unach.mx (H.H.T.-V.)
[5] Instituto de Energías Renovables-UNAM (IER-UNAM), Temixco 62580, Mexico; sjp@ier.unam.mx
* Correspondence: odin.reyes.v@cinvestav.mx

Abstract: Renowned for its versatility in environmental applications, biochar exhibits substantial potential to enhance anaerobic digestion, facilitate carbon sequestration, and improve water treatment through its highly efficient adsorption mechanisms. This study focuses on biochar derived from pineapple crown biomass, produced through slow pyrolysis, and its efficiency in removing organic dyes from contaminated water. The structural, morphological, and surface properties of both biochar and chemically activated biochar samples were comprehensively characterized using a range of techniques, including XRD, FTIR, XPS, BET surface area analysis, and SEM microscopy. The adsorption performance was evaluated using methylene blue (MB), rhodamine B (RhB), and malachite green (MG) dyes as model contaminants, with particular emphasis on the contact time on dye removal efficiency. Initial results showed removal rates of 10.8%, 37.5%, and 88.4% for RhB, MB, and MG, respectively. Notably, chemical activation significantly enhanced the adsorption efficiency, achieving complete (100%) removal of all tested dyes. Complete adsorption of MB and MG occurred within 9 min, indicating rapid adsorption kinetics. Adsorption data fit well with pseudo-second-order kinetics (R^2 = 0.9748–0.9999), and the Langmuir isotherm (R^2 = 0.9770–0.9998) suggested monolayer adsorption with chemical interactions between dyes and biochar. The intraparticle diffusion model further clarified the adsorption mechanisms. These findings demonstrate the efficacy of activated biochar for dye removal and highlight the potential of pineapple crown biomass in environmental remediation.

Keywords: biochar; adsorption; dye removal; pineapple crown biomass; environmental remediation

check for updates

Academic Editors: Konstantinos G. Kalogiannis and Maria Antoniadou

Received: 15 November 2024
Revised: 18 December 2024
Accepted: 25 December 2024
Published: 27 December 2024

Citation: Cano, F.J.; Reyes-Vallejo, O.; Sánchez-Albores, R.M.; Joseph, S.P.; Cruz-Salomón, A.; Hernández-Cruz, M.d.C.; Montejo-López, W.; González Reyes, M.; Serrano Ramirez, R.d.P.; Torres-Ventura, H.H. Activated Biochar from Pineapple Crown Biomass: A High-Efficiency Adsorbent for Organic Dye Removal. *Sustainability* **2025**, *17*, 99. https://doi.org/10.3390/su17010099

1. Introduction

Biochar, a carbonaceous material obtained by pyrolysis of biomass, has become a valuable resource in environmental applications due to its high porosity, structural stability, and diversity of functional groups on the surface [1]. This material, characterized by its high carbon content, can be produced from a wide range of organic waste, including coffee grounds [2], moringa leaves [3], pineapple peels [4], and others, thereby underscoring its versatility and sustainability. Among its numerous applications, biochar has demonstrated effectiveness in improving agricultural soil [5], the sequestration of carbon [6], and as a component in anaerobic digestion processes [7]. In the latter context, biochar plays a role in stabilizing microbial activity and optimizing biogas production in organic waste digestion systems, facilitating electron transfer, and mitigating process inhibitors such as ammonia and some volatile fatty acids.

One of the most promising emerging applications of biochar is in wastewater treatment, where its adsorption capacity allows for the efficient removal of both organic and inorganic pollutants [8]. The porous structure and functional groups provide active sites for the retention of toxic substances, facilitating the removal of heavy metals, dyes, pesticides, and pharmaceuticals present in industrial effluents [9]. These properties present in biochar render it a sustainable, high-performance adsorbent, offering significant advantages in terms of availability and ease of preparation. Furthermore, the characteristics of biochar, including specific surface area, pore size and volume, and functional group distribution, can be optimized through manufacturing conditions, which has a direct impact on its effectiveness as an adsorbent [10].

The adsorption capacity of biochar can be enhanced through the implementation of physical or chemical activation processes, which serve to augment the porosity and density of active sites on its surface [11,12]. In the case of chemical activation, the utilization of agents such as phosphoric acid or potassium hydroxide serves to enhance the adsorption capacity by inducing a structural expansion that allows for the formation of electrostatic interactions and hydrogen bonds with specific contaminants. Physical activation, which is typically conducted through heat treatment or exposure to steam, increases the specific surface area while maintaining a robust and stable structure [13]. It is important to distinguish activated biochar from activated carbon, as they differ in key aspects. Activated biochar is derived from renewable biomass sources and produced at lower temperatures during pyrolysis, making it a more sustainable and environmentally friendly option. In contrast, activated carbon is often produced from non-renewable sources, requiring more energy-intensive activation processes that result in a higher environmental footprint [14]. These distinctions highlight the environmental and cost-related advantages of activated biochar, which aligns with sustainability goals in adsorption technologies. The adsorption of pollutants such as heavy metals (e.g., lead and cadmium) [15] and the removal of organic dyes [16], which present an environmental risk due to their toxicity and persistence, have been demonstrated to be highly efficient in activated biochar. During the activation process, the incorporation of oxygenated functional groups facilitates the formation of bonds with polar pollutants [17,18], while the microporous structure and high surface area of the material allow the capture of non-polar pollutants through π–π and dispersion interactions [19].

While there are numerous photocatalytic nanomaterials (such as TiO_2, ZnO, $BiVO_4$, and CaO [20–22]) and advanced graphene-based composites [23] that are employed to degrade pollutants under UV irradiation, biochar is distinguished by its efficacy under ambient conditions without requiring external energy, which reduces operational costs and renders it an affordable and efficient option for pollutant removal.

This study examines the efficacy of biochar derived from pineapple crown biomass, produced via pyrolysis for the removal of organic dyes in aqueous solutions. The biochar samples and their activated variant were subjected to comprehensive characterization through a range of techniques, including X-ray diffraction (XRD), Fourier transform infrared spectroscopy (FTIR), X-ray photoelectron spectroscopy (XPS), Brunauer–Emmett–

Teller (BET) surface area analysis, and scanning electron microscopy (SEM). This novel approach enables the evaluation of the adsorption performance of activated biochar for model pollutants, including methylene blue (MB), rhodamine B (RhB), and malachite green (MG). It enables the analysis of the impact of contact time and the adsorption mechanisms involved, thereby contributing to the advancement of more efficient and sustainable environmental remediation technologies.

2. Materials and Methods

2.1. Preparation of Biochar and Activated Biochar

The biochar was synthesized by a controlled pyrolysis process. The pineapple crowns were first thoroughly washed with water to remove residual debris, followed by air drying for one week to reduce the surface moisture content. The biomass was then subjected to a second washing process and placed in an oven for drying at 65 °C for 48 h to achieve complete desiccation. The sieved biomass was then placed in a ceramic crucible and placed in a pyrolysis reactor with a constant nitrogen flow to ensure an inert atmosphere. The reactor was heated to a target temperature of 450 °C at a controlled heating rate of 10 °C/min and maintained at this temperature for one hour to facilitate thermal decomposition of the organic matter. Following the pyrolysis process, the reactor was allowed to cool to ambient temperature. Finally, the resulting biochar was ground using a mortar to achieve a homogeneous powder.

Subsequently, the activation process followed an eco-friendly method adapted from established protocols for graphene oxide synthesis [24,25]. The activation procedure commenced with the preparation of a mixed acid solution, consisting of 43.2 mL of concentrated sulfuric acid (H_2SO_4, ACS reagent, 95.0–98.0%, Sigma-Aldrich, St. Louis, MO, USA) and 4.8 mL of concentrated orthophosphoric acid (H_3PO_4, 85%, Sigma-Aldrich, USA). This acid mixture was then gradually added to 1 g of biochar powder under continuous stirring for 3 h while maintaining the system in a cold bath at 4 °C to ensure temperature control and prevent exothermic reactions. At this stage, the acid mixture promotes the expansion of biochar sheets, increases surface area, and enhances interactions with the oxidizing agent. Following this, 6 g of potassium permanganate ($KMnO_4$, 99.0%, ACS reagent, Sigma-Aldrich, USA) was introduced into the reaction mixture, which serves as the primary oxidizing agent, introducing oxygen-containing functional groups to the biochar surface. The reaction continued for 2 h. After this period, a solution containing 12 mL of hydrogen peroxide (H_2O_2, 30 wt.%, ACS reagent, Sigma-Aldrich, USA) and 13 mL of hydrochloric acid (HCl, 36.5–38.0%, ACS reagent, Sigma-Aldrich, USA) was added dropwise to the mixture under vigorous stirring for 30 min. This mixture of H_2O_2 and HCl was used specifically to stop the oxidation reaction by decomposing residual $KMnO_4$. The exfoliation of the treated material was then performed through sonication for 30 min. Following exfoliation, the resulting dispersion was subjected to multiple washing cycles until the supernatant reached a neutral pH (7). Finally, the material was collected and dried in an oven at 65 °C for 12 h to yield the activated biochar. The stages of this oxidation mechanism are detailed in our previous study [26], which provided the foundational basis for this methodology.

2.2. Characterization of Materials

X-ray diffraction (XRD) analysis was performed using a Bruker D2 PHASER diffractometer (Bruker Corporation, Billerica, MA, USA), employing Cu-Kα radiation (λ = 1.54056 Å) with an operating voltage of 40 kV and a current of 30 mA. The diffraction patterns were collected in the 2θ range of 10° to 60°, with a scanning rate of 2°/min, to characterize the crystalline structure of the materials. Fourier-transform infrared (FTIR) spectroscopy was carried out on a PerkinElmer Frontier FTIR spectrometer (PerkinElmer, Inc., Waltham, MA, USA), equipped with a diamond attenuated total reflectance (ATR) accessory. Spectral data were acquired within the 580–4000 cm^{-1} range, with a resolution of 4 cm^{-1}, enabling the identification of characteristic functional groups within the samples. X-ray photoelectron spectroscopy (XPS) was conducted using a PHI VersaProbe II system (ULVAC-PHI, Inc., Chanhassen, MN, USA), operating under a vacuum pressure of 2×10^{-8} mTorr. Monochromatic X-ray radiation from an aluminum anode (1486.6 eV) was used to analyze the surface chemical composition and oxidation states of the materials. Scanning electron microscopy (SEM) imaging was performed with a Hitachi S5500 field-emission scanning electron microscope (FESEM-Hitachi High-Technologies Corporation, Tokyo, Japan) at an accelerating voltage of 5 kV, providing high-resolution images of the surface morphology of the samples. The specific surface area and pore volume of the materials were determined via nitrogen adsorption measurements using the Brunauer–Emmett–Teller (BET) method on a Micromeritics Gemini 3240 instrument (Micromeritics Instrument Corporation, Norcross, GA, USA). Before analysis, the samples were degassed at 150 °C for 12 h under a nitrogen flow to eliminate adsorbed moisture and volatile contaminants.

2.3. Adsorption Procedure

Adsorption experiments were conducted in batch mode, utilizing 100 mL of 10 ppm solutions of each dye (MB, RhB, and MG) and 0.1 g of biochar and activated biochar powders, respectively. For each compound, the mixture was subjected to vigorous stirring in the dark for 30 min to ensure adequate contact between the adsorbent and the dye molecules. All experiments were conducted at a neutral pH (~7) and room temperature to ensure consistency and neutrality in the adsorption behavior of the dyes. At specified intervals (every 3 min), aliquots were withdrawn, centrifuged immediately, and analyzed using a UV–Vis spectrophotometer JASCO model V-670 (JASCO Corporation, Tokyo, Japan), to determine the concentration of the dyes over time. The maximum absorbance wavelengths were selected as 664 nm for MB, 617 nm for MG, and 555 nm for RhB, with deionized water used as the reference. The effect of biochar activation on the dye removal efficiency in solution was evaluated. Removal efficiency, R (%), and equilibrium adsorption capacity, q_e (mg/g), were calculated using the following equations:

$$R\ (\%) = \left(\frac{C_0 - C_e}{C_0} \right) \times 100 \tag{1}$$

$$q_e = \left(\frac{C_0 - C_e}{W} \right) \times V \tag{2}$$

where C_0 and C_e (mg/L) are initial and equilibrium concentrations of dye, respectively, W (g) is the mass of adsorbent, and V (L) is the volume of the solution.

The adsorption kinetic experimental data were fitted and analyzed using pseudo-second-order kinetic and intra-particle diffusion equations.

$$\textit{Pseudo-second-order kinetic}: \ \frac{t}{q_t} = \frac{1}{k_2 q_e^2} + \frac{1}{q_e} t \tag{3}$$

$$\textit{Intra-particle diffusion model}: \ q_t = k_{id} t^{1/2} + C \tag{4}$$

where q_t (mg/g) stands for the adsorption capacity at time *t*; k_2 (g/mg/h) represents the adsorption rate constants of pseudo-second-order kinetics; k_{id} (mg/[g·$\text{min}^{1/2}$]) is the intraparticle diffusion rate constant; C is a constant related to the thickness of the boundary layer.

The isothermal adsorption experiment data were fitted and analyzed using the Langmuir model. The fitting equations are as follows:

$$Langmuir model: \frac{1}{q_e} = \frac{1}{q_{max}K_L} \cdot \frac{1}{C_e} + \frac{1}{q_{max}} \tag{5}$$

where q_{max} (mg/g) represents the maximum adsorption capacity when adsorption equilibrium is reached; K_L (L/g) is the adsorption constant of the Langmuir equation. The Langmuir isotherm can be discussed in terms of the dimensionless constant, R_L which is calculated by using the following equation:

$$R_L = \frac{1}{(1 + C_0K_L)} \tag{6}$$

3. Results and Discussion

3.1. Chemical Composition

XPS characterization was employed to determine both the elemental composition and the predominant chemical states on the surface of the biochar (Figure 1a). The spectra of both materials showed significant signals in the C *1s* and O *1s* regions. After activation, the relative oxygen content increased significantly from 13.36% to 49.13%, as reflected by a substantial rise in the O/C ratio, from 0.17 to 1.80. This increase confirms the incorporation of oxygenated functional groups on the surface of the activated biochar, indicating that the elemental composition of both materials is primarily carbon and oxygen. Deconvolution of the C *1s* spectrum of the activated biochar (Figure 1b) revealed peaks with binding energies at 286.16, 287.49, and 289.04 eV associated with C-O, C=O, and -COOH bonds, respectively. These energy values are consistent with those reported in previous studies and support the identification of these oxygenated functional groups that enhance surface reactivity [27].

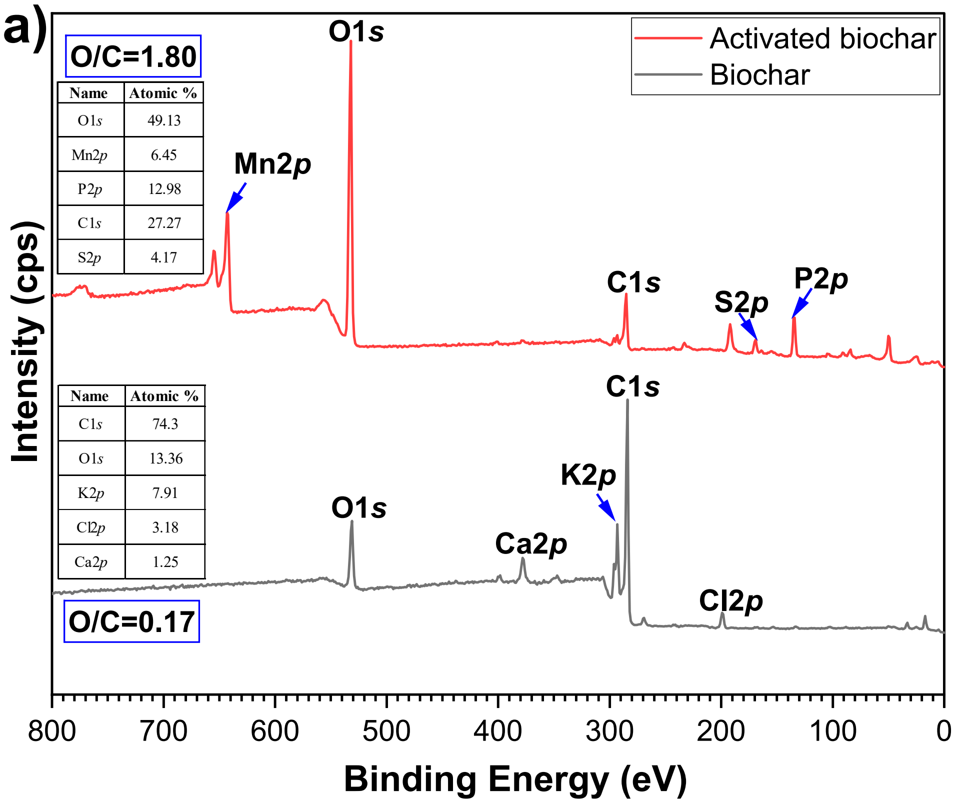

Figure 1. *Cont.*

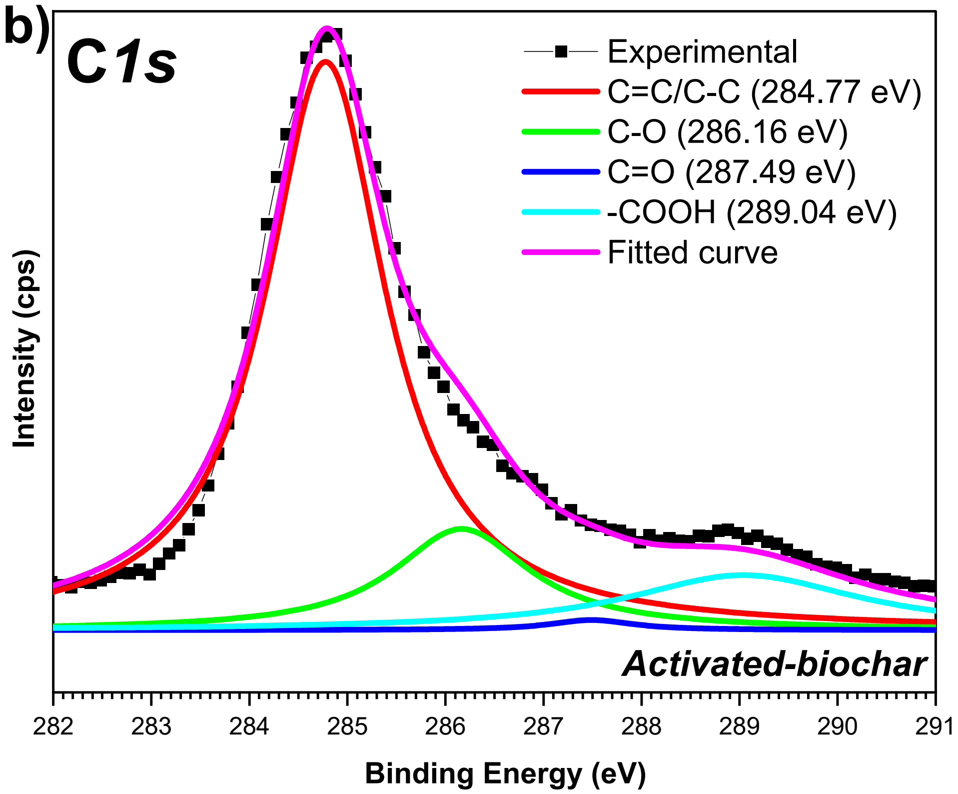

Figure 1. (**a**) XPS spectra of biochar and activated biochar, (**b**) deconvolution of the C *1s* spectrum of the activated biochar.

In the spectrum of the biochar, additional signals were detected in the Ca *2p* regions, indicating the presence of calcium-derived compounds, along with contributions from K *2p* and Cl *2p*, which together accounted for 23.6% by mass. After activation, these signals disappear, suggesting that they originated from surface-adsorbed species that were destabilized and subsequently removed during the chemical treatment process. Additionally, new signals were detected in the activated biochar in the Mn *2p*, S *2p*, and P *2p* spectral regions, attributed to impurities introduced during the activation process with $KMnO_4$ as the oxidizing agent and H_3PO_4 and H_2SO_4 as acidic components. These impurities, which constitute 12.34% by mass, may act as additional surface-active sites, enhancing dye adsorption capacity [28]. Nevertheless, the presence of elements such as manganese may also alter the electronic structure of the material, potentially impairing its performance in specific applications [29].

FTIR spectroscopy was employed as a complementary technique to XPS analysis, allowing a more complete evaluation of the surface chemistry of the material. Figure 2 shows the FTIR spectra of the biochar and activated biochar, highlighting several characteristic bands in the infrared region that correspond to specific functional groups in their structure. The band at 3778 cm^{-1} corresponds to the free stretching of hydroxyl (OH) groups on the biochar surface. These groups are not involved in hydrogen bonding, which gives rise to a distinct band in this region. Similarly, the band at 3107 cm^{-1} is attributed to the stretching of C-H bonds in double bonds (C=CH), indicating the presence of aromatic compounds or alkenes, which are characteristic of the carbonaceous structure of biochar.

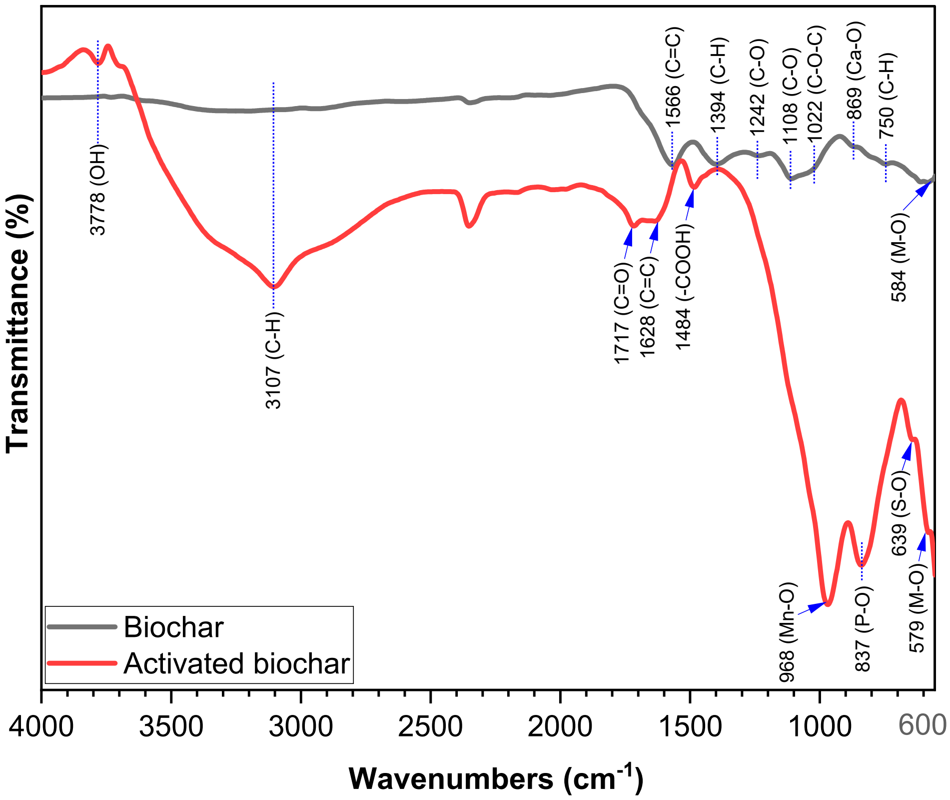

Figure 2. FTIR of biochar and activated biochar.

The spectrum of biochar exhibits bands associated with aromatic ring vibrations C=C at 1566 cm^{-1} [30], indicative of aromatic compounds formed during biomass pyrolysis. This indicates that biochar retains some structural integrity of the original organic matter, particularly lignin, which is rich in aromatic structures. In addition, bands at 1394 cm^{-1} and 750 cm^{-1} were associated with out-of-plane bending vibrations of C-H bonds in aromatic rings. The bands at 1232 cm^{-1}, 1108 cm^{-1}, and 1022 cm^{-1} are attributed to C-O or C-O-C bond stretching vibrations present in alcohols, ethers, or polysaccharide-derived compounds such as hemicellulose and residual cellulose [31,32]. These features indicate the presence of oxygenated compounds derived from lignin or partially decomposed cellulose during pyrolysis. Furthermore, the band at 869 cm^{-1} is assigned to Ca-O bonds, while the band at 584 cm^{-1} may correspond to metal–oxygen bond vibrations (M-O) [33], specifically from K-O or Ca-O bonds, as corroborated by XPS analysis.

For the activated biochar, the oxidation process induced significant changes in its chemical structure and surface functionality, as evidenced by the appearance of new bands in the infrared spectrum. This process increased the concentration of oxygenated groups, such as carbonyls (C=O), reflected in the band at 1717 cm^{-1} characteristic of carboxylic groups (-COOH), ketones, and aldehydes. Oxidation also modified the aromatic structure of the biochar, shifting the C=C stretching band to 1628 cm^{-1} due to the incorporation of new functional groups. This shift results from the impact of oxygenated groups on the π-bond system of aromatic structures, where alterations in electron density disrupt the conjugation of C=C bonds, leading to higher vibrational frequencies. This phenomenon is consistent with the literature reports describing how the oxidation of aromatic compounds affects π-bond conjugation, shifting C=C bands toward higher frequencies [34]. Additionally, the band at 1484 cm^{-1}, associated with the vibration of C=C bonds in aromatic rings and carboxylic groups, shows variations in intensity and position, indicating chemical transformation in the bond network of the material. Oxidation also enhances the bands at 968 cm^{-1}, attributed to the vibration of Mn-O bonds, suggesting the incorporation of manganese oxides (MnO_2, Mn_2O_3) on the biochar surface. The presence of phosphorus was evidenced by the band at 837 cm^{-1} corresponding to P-O vibrations, indicating the formation of phosphate groups, while the band at 639 cm^{-1} associated with S-O bonds suggests the introduction of sulphonate groups.

Activation with $KMnO_4$ creates oxidized active sites on the biochar surface, which increases the density of Mn, P, and S functional groups in the activated areas. These groups, being dispersed on the surface, enhance the infrared signal of their bonds in the FTIR spectrum. Although the total concentrations of Mn, P, and S are moderate, the high intensity of their bands is explained by their surface concentration and a favorable chemical environment that enhances the infrared response. This phenomenon confirms that the $KMnO_4$ activated biochar has a surface enriched in oxidized species, suggesting a higher reactivity.

3.2. Microstructure

Figure 3 presents the X-ray diffraction (XRD) patterns for the biochar and activated biochar samples. The diffractogram of the biochar shows two characteristic peaks at 24.0° and 40.7°, indicative of graphitization during biomass pyrolysis [35]. The signal at 24.0° corresponds to the (002) reflection, associated with the stacked aromatic layers of graphite [36]. The amplitude of this signal suggests a reduction in crystallite dimensions perpendicular to the layers, indicating that pyrolysis produces disordered graphitic domains rather than highly ordered graphite. The signal at 40.7° corresponds to the (100) plane, reflecting the sp^2 hybridization of the carbon atoms [37] and providing further insights into the structural order of the biochar.

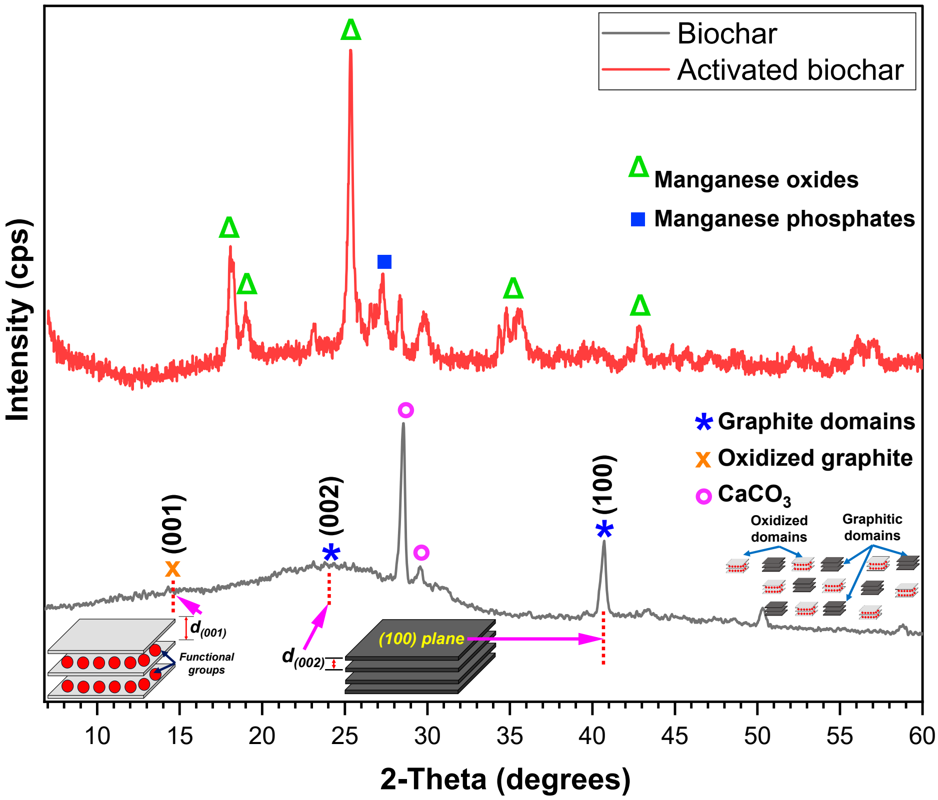

Figure 3. XRD pattern of biochar and activated biochar.

In addition, a broad signal around 14.8° is observed, typically associated with interlayer spacing in graphite-like materials, influenced by the presence of oxygenated functional groups located between the layers. This signal, characteristic of materials such as graphene oxide (GO), reflects an increase in interlayer spacing compared to graphite, suggesting structural heterogeneity in the biochar. For GO, the (001) signal is generally observed in the 9° to 15° range [38]; therefore, the signal in biochar likely indicates variability in the concentration and distribution of oxygenated groups, resulting in a structure intermediate between graphite and GO. The coexistence of signals (indicative of crystalline graphite domains) and broader, functionalized signals (typical of GO) suggests that biochar consists of a mixture of stacked crystalline regions and heavily functionalized domains. Some regions exhibit dense functionalization, whereas others retain minimal oxidation, which contributes to the heterogeneous structure of the material [39]. This structural inhomogeneity may be influenced by the pyrolysis conditions, which promote an uneven distribution of oxygenated functional groups between the carbon layers. Additionally, signals at 28.5° and 29.5° are attributed to carbonate minerals, such as calcite ($CaCO_3$) (JCPDS file n°. 47–1743) [40], confirming the presence of inorganic impurities in limited quantities.

On the other hand, the activated biochar shows significant structural changes compared to its non-activated counterpart. The disappearance of graphite signals is indicative of the rapid oxidation and reduction in the size of the crystalline graphite domains. The activation process increases the interplanar distance and promotes the exfoliation of the layers, which results in a more amorphous structure enriched with oxygenated functional groups [26]. If the exfoliation progresses to the point of separating the layers into single monolayers, the characteristic signal of the (001) plane diminishes or disappears entirely, explaining its absence in the diffractogram of the activated biochar. Furthermore, distinct signals corresponding to the formation of manganese oxides (such as MnO_2 and Mn_2O_3) and manganese phosphates ($MnPO_4$) were observed, confirming the Mn and P presence identified through XPS analysis. These findings underscore the profound structural and chemical modifications induced by chemical activation, yielding an activated biochar characterized by a highly functionalized surface and a disordered structure—key attributes of materials with high surface reactivity [12].

3.3. Morphology and Specific Surface

SEM images at different magnifications, shown in Figure 4, provide detailed insights into the morphology of the biochar before and after chemical activation, revealing significant changes in its structure. The biochar in Figure 4a displays large blocks with stacked lamellae, indicative of a layered structure typical of carbon-rich materials derived from biomass pyrolysis [41]. These lamellae exhibit an interlocking texture, forming irregular layers, suggesting an organized structure with high carbon content, similar to the morphology of graphite-based materials [42,43]. This morphology is consistent with the findings reported by de Almeida, S. G., 2022 for a biochar produced from sugarcane biomass [44]. At higher magnifications, the biochar surface reveals a homogeneous distribution of small particles and flake-like fragments, likely resulting from thermal degradation during pyrolysis. This process facilitates the gradual decomposition of the microstructure, increasing surface roughness and generating smaller particles and flakes [45]. The SEM images confirm the presence of large, rough carbon flakes with smaller fragments adhered to their surfaces, clearly visible in the basal planes of the blocks.

On the other hand, chemical activation induces significant morphological changes in the biochar (Figure 4b), notably altering its surface structure. In contrast to the layered structure of the initial biochar, the activated biochar exhibits a morphology composed of smaller, rougher particles ranging in size from 800 to 900 nm. This transformation suggests a fragmentation of the original structure and a pronounced increase in surface roughness. At higher magnifications, the surface of these particles reveals flake-like features similar to those observed in the biochar, indicating a process of exfoliation and fragmentation of the graphitic lamellae caused by chemical attack [46], as corroborated by the XRD pattern. The chemical attack weakens the bonds between graphite layers, promoting the formation of smaller fragments, which then agglomerate into rough, flaky particles. This process contributes to an increase in the specific surface area of the activated biochar, as reflected in the values in Table 1.

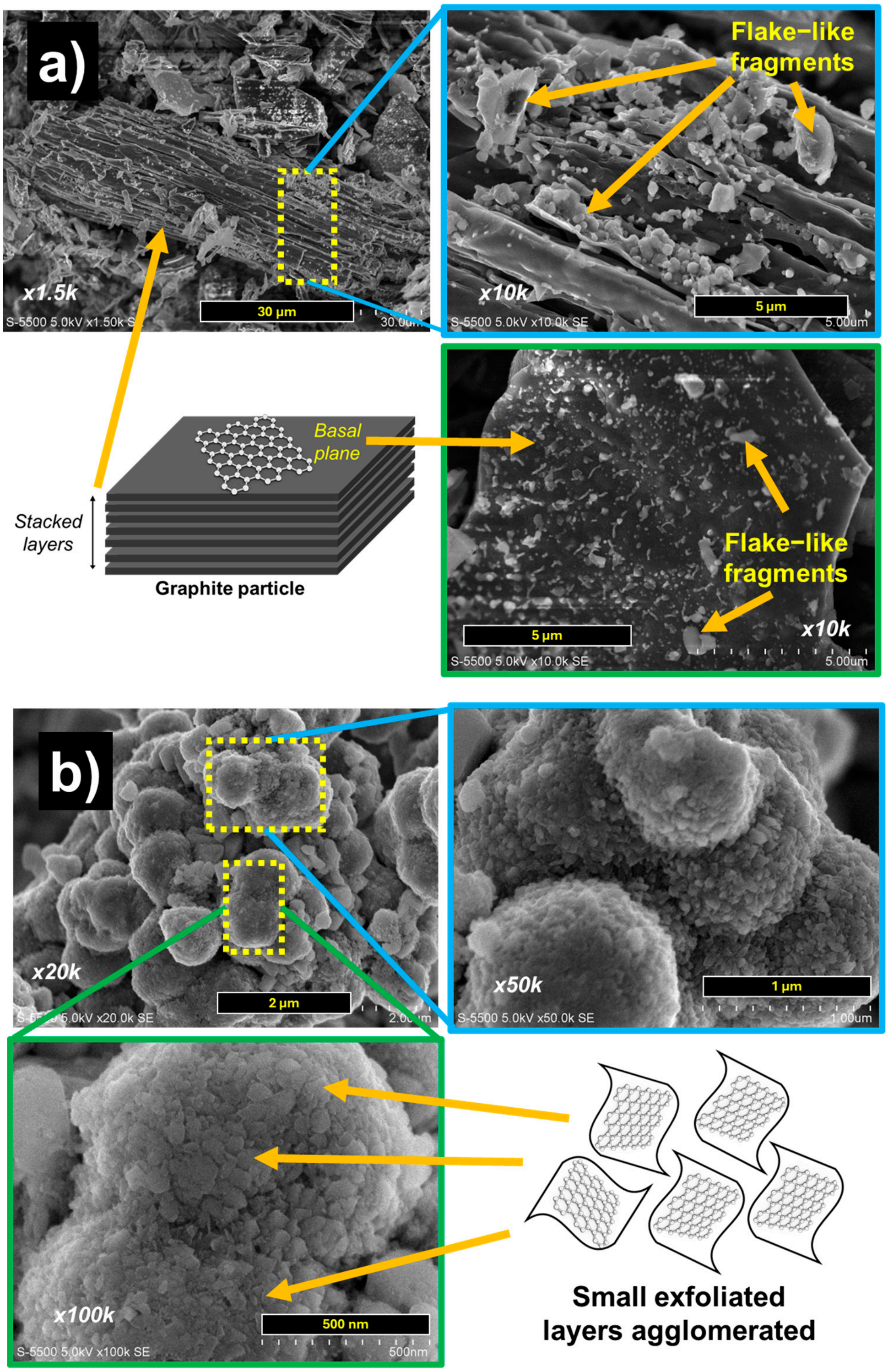

Figure 4. SEM images of (**a**) biochar and (**b**) activated biochar.

Table 1. Specific surface area (SSA) and pore volume of biochars.

Material	Specific Surface Area BET (m^2/g)	Pore Volume (cc/g)
Biochar	2.60	0.142
Activated biochar	3.25	0.011

Despite these morphological changes, the increase in SSA was moderate. The high concentration of oxygenated functional groups on the surface of activated biochar facilitates the agglomeration of exfoliated and fragmented lamellae [47]. Thus, although chemical activation increased roughness and generated flaky structures on the surface, the resulting agglomeration prevented a more significant increase in total surface area. On the other hand, the observed reduction in pore volume could be due to the partial collapse of the pore structure during the chemical treatment, especially affecting the micropores by restructuring or destruction of the internal network. The agglomeration of carbon fragments on the surface may obstruct access to deeper pores, reducing the space available for adsorption [48]. In addition, the introduction of oxygenated functional groups on the pore walls occupies space within the pores, decreasing the effective volume, which may potentially limit the adsorption of larger molecules [49]. However, although the reduction in pore volume may limit its adsorption capacity for large molecules, the slight increase in surface area, together with the presence of active oxygenated groups, may favor the adsorption of smaller and polar compounds, optimizing its application in water remediation.

3.4. Adsorption Experiments

3.4.1. Effects of Contact Time and Kinetics

The adsorption efficiency of dyes on biochar and activated biochar was evaluated as a function of contact time for 30 min under dark conditions. This parameter is critical in determining how quickly the molecules of dye are captured by the adsorbent surface, as well as the time required to reach adsorption equilibrium. For a more rigorous analysis of the kinetics, the results were evaluated at defined time intervals and fitted to both pseudo-first-order and pseudo-second-order adsorption kinetic models. However, the R^2 values demonstrated a more suitable fit of the experimental data to the pseudo-second-order model, indicating that it better describes the adsorption process. Nevertheless, the parameters obtained from the pseudo-first-order model are provided in Table S1 as a reference.

Figure 5a exhibits varying adsorption efficiencies on biochar. For RhB, removal reached 10.8%; for MB, 37.5%; and for MG, 88.4% after 30 min. These results are attributed to the structure and chemical composition of the biochar surface, as confirmed by FTIR and XPS analyses. The limited presence of functional groups, such as hydroxyl (-OH) and carboxyl (-COOH), which are essential for electrostatic interactions and hydrogen bonding [50], explains the moderate adsorption rates for all dyes. Regarding the observed differences in removal percentages among the dyes, these variations were attributed to the distinct physicochemical properties of each dye.

Although the dyes are cationic and the biochar surface lacks sufficient oxygenated functional groups for effective electrostatic interactions, MG showed significantly higher adsorption efficiency. This superior performance is likely due to the planar structure of the aromatic rings of the MG molecule, which allows stable π–π stacking interactions with the adsorbent [51]. It has been previously demonstrated that π–π interactions can possess a chemical character as a consequence of electron transfer and a particular affinity between the adsorbent and the adsorbate [52,53]. These interactions, which are stronger and more stable compared to those with MB, are enhanced by the molecular complexity of MG and its nitrogen atom, which disrupts the electronic conjugation of MB, thereby reducing the stability of its interactions [54]. Furthermore, the larger and more complex structure of MG allows it to form multiple π–π interactions more effectively than MB, which is smaller and less conjugated [55,56]. This enhances the ability of MG to exploit the graphitized regions of the biochar surface, promoting more intense and stable interactions. In contrast, RhB showed significantly lower adsorption due to its pH sensitivity. In neutral media, weakened cationic interactions limited its removal efficiency [57]. This aligns with previous studies reporting that RhB adsorption is almost entirely inhibited at pH > 6 [58]. These findings underscore the importance of both the chemical and structural properties of the adsorbent and the intrinsic characteristics of the dyes in determining adsorption performance. Figure 6 provides a schematic representation of the potential interactions between the dyes and the active sites of the biochar surface. These interactions are proposed based on comprehensive studies reported in the literature, which have compared the chemical bonds formed between similar adsorbents and adsorbates after the adsorption process [56,59,60]. These studies utilize advanced characterization techniques such as FTIR to confirm the nature of these interactions. The schematic emphasizes key mechanisms such as π–π stacking interactions, hydrogen bonding, electrostatic attractions, and van der Waals forces, highlighting the role of the functional groups present on the biochar surface and the molecular structure of the dyes.

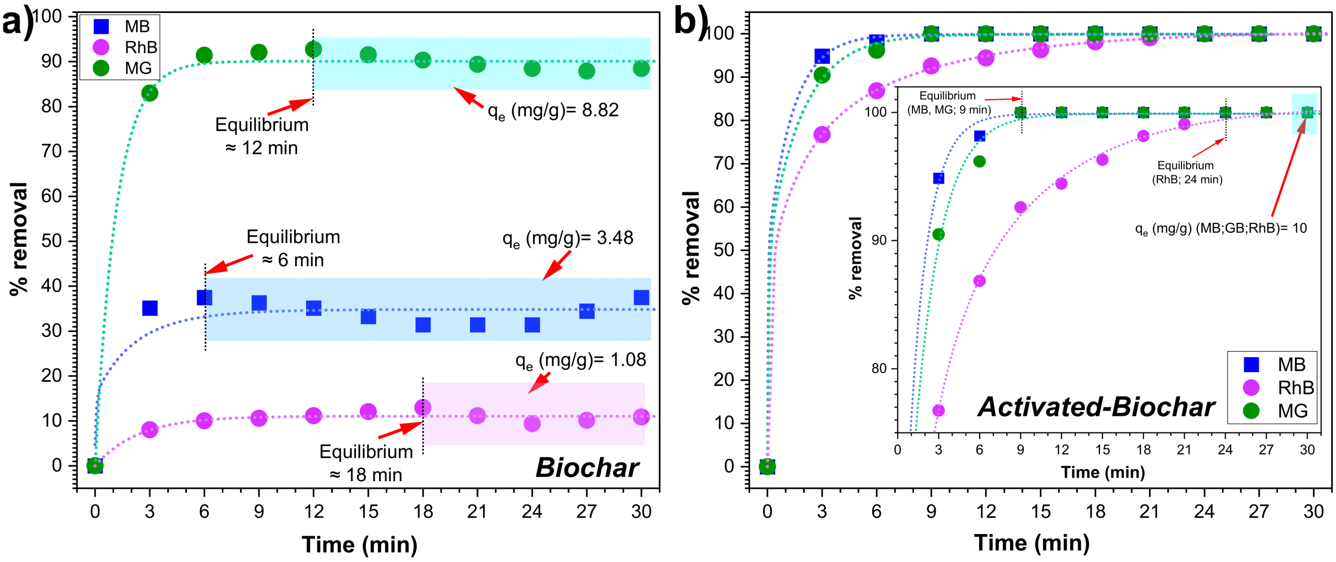

Figure 5. Effect of contact time on dye adsorption on (**a**) biochar and (**b**) activated biochar (under working conditions: initial dye concentration: 10 ppm, adsorbent dosage: 1 g/L, pH: 7, room temperature).

The activated biochar (Figure 5b) exhibited a significant improvement in adsorption efficiency, reaching a complete removal (100%) of the three evaluated dyes. This enhancement is attributed to the substantial increase in the concentration of oxygenated functional groups, which increases both the polarity and reactivity of the biochar surface, making the improvement in RhB adsorption more evident. Despite a reduced pore structure (confirmed by BET), the higher concentration of oxygenated functional groups and the presence of impurities compensate for this limitation by providing additional active sites, enabling rapid and effective interactions with the dyes. However, the time required to reach adsorption equilibrium varied among the dyes. While MB and MG reached equilibrium within 9 min, RhB required significantly more time (24 min). This disparity suggests that adsorption kinetics depend not only on the surface properties of the adsorbent but also on the molecular structure and polarity of the dyes. RhB, with its larger molecular size and reliance on polar interactions, requires more time to establish electrostatic stabilization and form hydrogen bonds with the oxygenated functional groups on the biochar surface. This behavior aligns with previous studies comparing the adsorption capacity of various biomass-derived biochars, thus supporting the findings obtained in this work within the existing literature. Table S2 provides a detailed comparison of recent studies investigating the removal of aquatic pollutants using biomass-derived biochars, highlighting the influence of surface structure and functional groups on adsorption performance. This broader context strengthens the understanding of how chemical modifications in biochars enhance their adsorption efficiency for diverse contaminants.

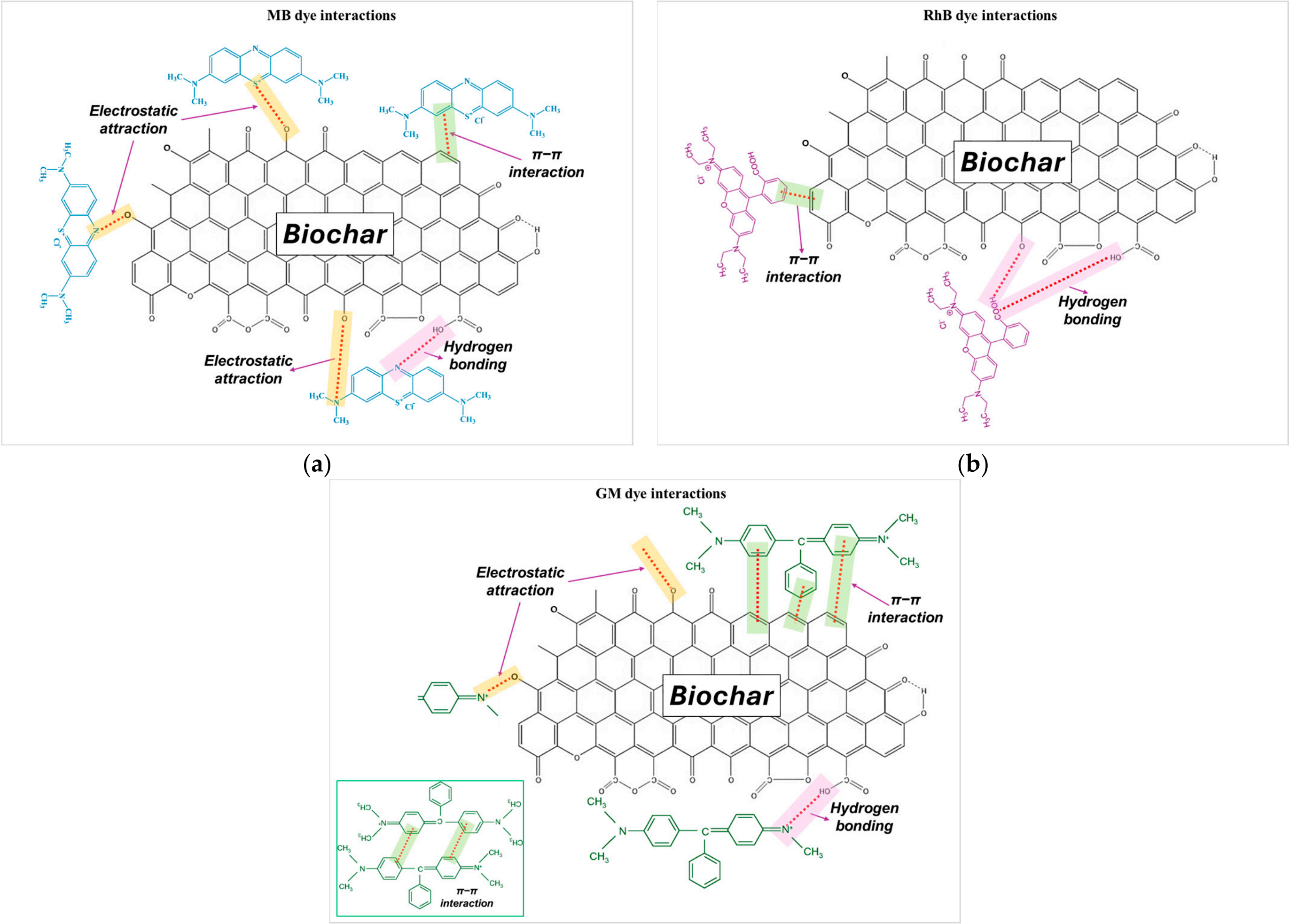

(**a**) (**b**)

(**c**)

Figure 6. Representation of the potential interactions between biochar and (**a**) MB, (**b**) RhB, and (**c**) MG. The structural models were adapted from references [53,56,59,60].

Figure 7 illustrates that the pseudo-second-order kinetic model provides the best fit for describing the adsorption process in all cases, highlighting the predominance of chemisorption. This implies that the adsorption rate is primarily governed by the availability of active sites and electron exchange interactions between the dye molecules and the oxygenated functional groups on the biochar surface, rather than being limited solely by diffusion processes [61]. The kinetic parameters derived from the model are summarized in Table 2, providing quantitative insights into the adsorption dynamics for each dye.

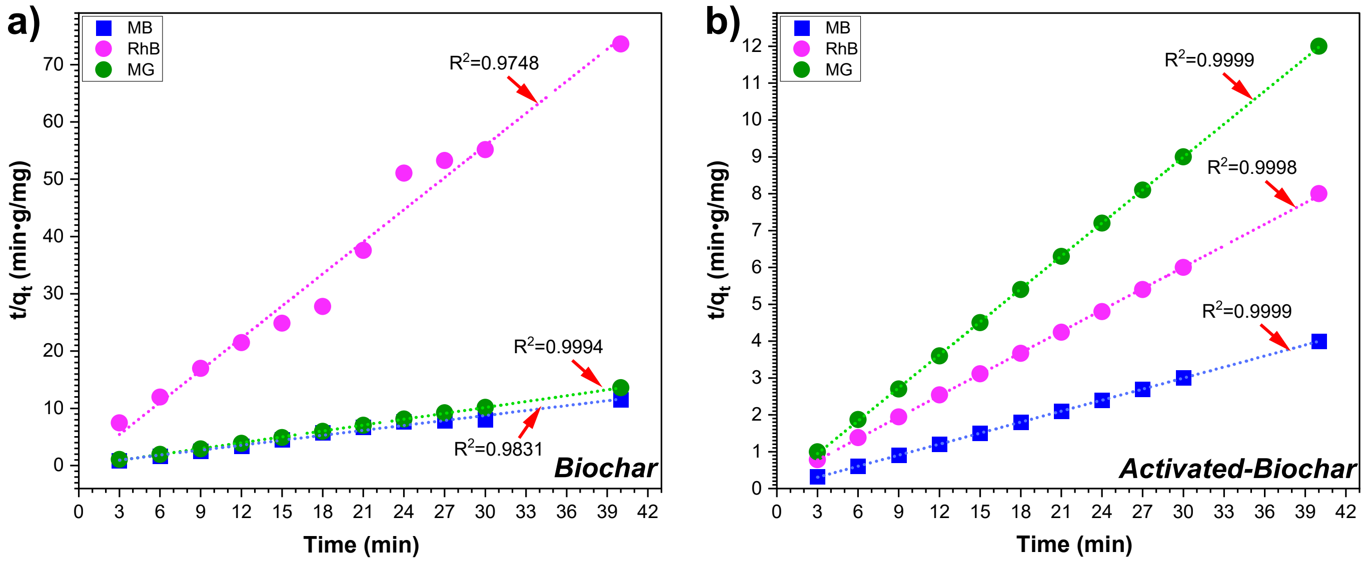

Figure 7. Pseudo-second-order kinetic study of dye adsorption by (**a**) biochar and (**b**) activated biochar.

Table 2. Results of the pseudo-second-order kinetic model for the adsorption of biochar and activated biochar.

Material	Dye	q_e (mg/g)$_{\text{(Experimental)}}$	Pseudo-Second Order		
			k_2 (min^{-1})	q_e (mg/g)$_{\text{(Calculated)}}$	R^2
Biochar	MB	3.48 ± 0.04	0.76	3.47	0.9831
	RhB	1.08 ± 0.02	10.22	1.07	0.9748
	MG	8.82 ± 0.11	0.35	8.77	0.9994
Activated biochar	MB	10 ± 0.06	1.18	10.03	0.9999
	RhB	10 ± 0.50	0.10	10.32	0.9998
	MG	10 ± 0.12	0.58	10.06	0.9999

3.4.2. A Mechanistic Model for MB Dye Diffusion

To further elucidate the complex adsorption mechanisms observed, an intraparticle diffusion model was applied to analyze the transport and diffusion processes of species within the adsorbent materials [62]. Plots of q_t versus $t^{1/2}$ for the dyes adsorbed on biochar and activated biochar are presented in Figure 8, fitting a linearized form of the model to describe each adsorption phase [63]. The adsorption process for all three dyes comprises three distinct stages.

In the first stage (I), rapid and pronounced adsorption occurs within the initial three minutes of contact, particularly for all three dyes. During this stage, adsorption approaches near-maximum levels, attributed to the high availability of surface-active sites and the steep concentration gradient between the dye molecules in the solution and the adsorbent surface. This phase is dominated by surface adsorption, where dye molecules rapidly bind to accessible outer surface sites on the biochar, unhindered by internal diffusion constraints, enabling near-complete adsorption within a short time.

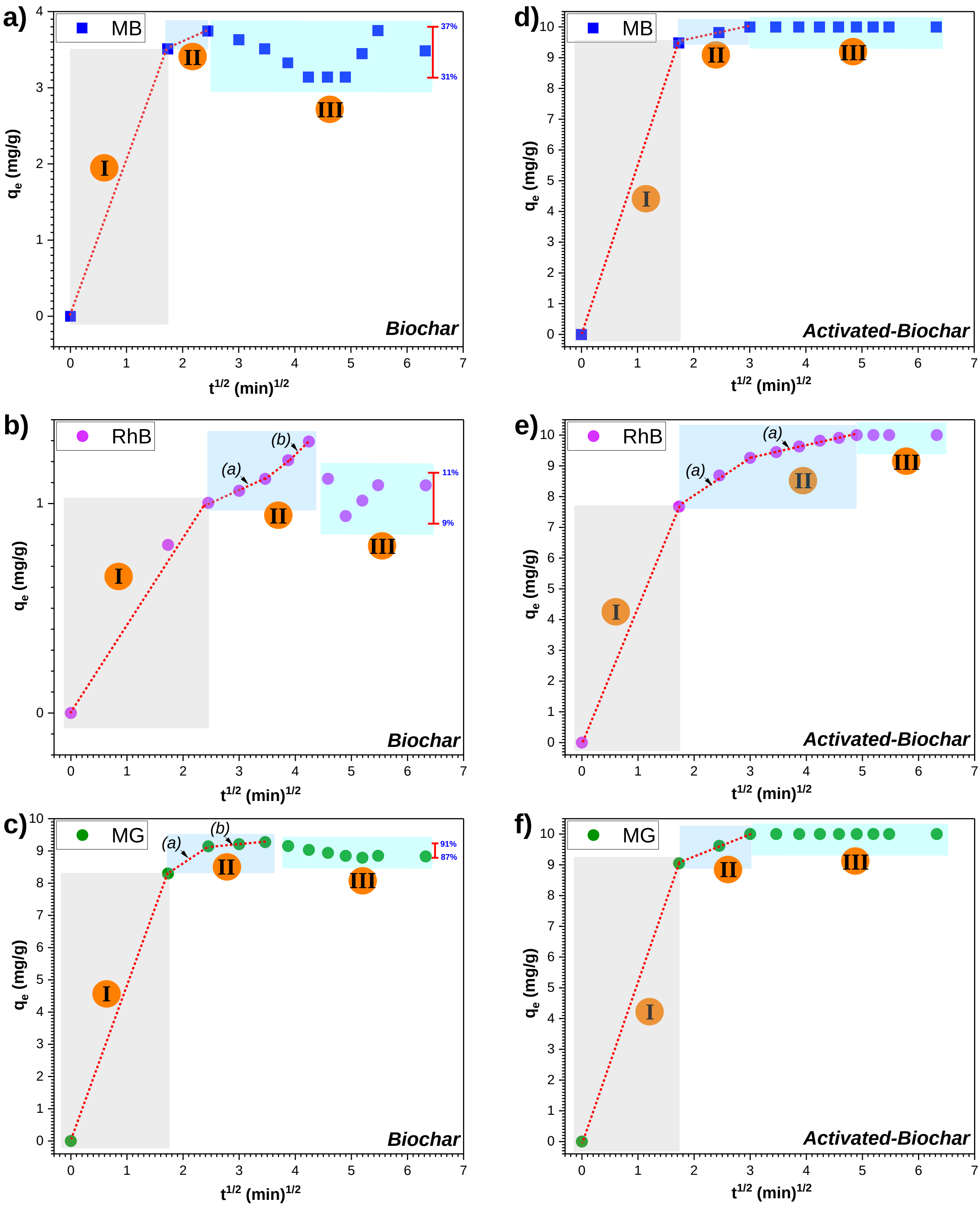

Figure 8. Intraparticle diffusion model for dye adsorption in (**a**–**c**) biochar and (**d**–**f**) activated biochar.

In the second stage (II), the adsorption continues at a slower rate because the surface sites have been occupied, causing the process to become limited by intra-particle diffusion into the deeper pores. The penetration of the dye molecules into the internal structure increases resistance to diffusion, limiting the rate of adsorption. Each dye reaches equilibrium during this phase, influenced by its molecular properties. For biochar, MB reaches equilibrium quickly (≈6 min), likely due to its smaller molecular size and favorable diffusion characteristics, whereas RhB and MG equilibrate at ≈18 and 12 min, respectively, due to their larger size and higher resistance to internal diffusion. On activated biochar, equilibrium is reached slightly later, with MB and MG equilibrating at 9 min and RhB at 24 min. The slower rate in this phase reflects the diffusion-limited nature of the process [61]. Interestingly, within this second stage, the presence of two linear sub-regions (*a* and *b*) suggests a transition between two diffusion phases, specifically for RhB and MG: an initial faster diffusion into larger, more accessible pores, followed by a slower diffusion into smaller or less accessible pores. The structural heterogeneity of the materials, combined with the molecular size and interaction of the dyes with the pore walls, likely influenced this phenomenon.

Finally, in the third stage (III), after the maximum adsorption is achieved, biochar (Figure 8a–c) exhibits a slight desorption followed by readsorption. For MB, the desorption–readsorption cycle ranges between 31% and 37%, while for RhB and MG, the values are 9–11% and 87–91%, respectively. This stage reflects a dynamic equilibrium, where a fraction of the adsorbed molecules undergo desorption, which can be attributed to the presence of physisorption interactions. This allows for a limited degree of reversibility. Although kinetic models indicate that the process is dominated by chemosorption, the presence of multiple interactions—such as π–π stacking, van der Waals forces, and hydrogen bonding (as depicted in Figure 6)—suggests a hybrid adsorption mechanism involving both chemisorption and physisorption. Therefore, the term 'chemosorption' in this context refers to specific interactions involving electronic affinities beyond weak physical forces. In contrast, activated biochar demonstrates significantly improved adsorption behavior (Figure 8d–f). During the third stage, no desorption is observed, indicating irreversible adsorption and a stronger predominance of chemisorption. This enhanced performance is attributed to the increased concentration of oxygenated functional groups and structural modifications introduced during activation, which strengthen the adsorbent–dye interactions and improve the stability of adsorption.

The parameters of the intraparticle diffusion model, presented in Table 3, indicate that the intraparticle diffusion rate constant $k_{p1} > k_{p2}$, confirms that the rate of dye removal during the first stage is higher than in the second stage for both systems [64].

Table 3. Stage parameters of intraparticle diffusion kinetics model for biochar and activated biochar adsorption.

Material	**Dye**	**1st Step**		**2nd Step**		**3rd Step**	
		k_{p1} (mg/g·min$^{1/2}$)	**R^2**	**k_{p2} (mg/g·min$^{1/2}$)**	**R^2**	**k_{p3} (mg/g·min$^{1/2}$)**	**R^2**
Biochar	MB	2.028	1	1.6959	1	-	-
	RhB	0.413	0.9805	(*a*) 0.112 (*b*) 0.229	0.995 0.998	-	-
	MG	4.791	1	(*a*) 1.176 (*b*) 0.129	1 0.995	-	-
Activated biochar	MB	5.476	1	3.916	0.992	-	-
	RhB	4.430	1	(*a*) 1.259 (*b*) 0.401	0.986 0.988	-	-
	MG	5.224	1	3.846	0.998	-	-

3.4.3. Adsorption Isotherm Models

To further understand the adsorption behavior of dyes on biochar and activated biochar, the experimental data were fitted to both the Freundlich and Langmuir isotherm models. While the analysis of the Freundlich model is included in the supplementary material (Figure S1), the R^2 values confirm that the Langmuir model provides a superior fit to the experimental data. This result indicates that dye adsorption on biochar and activated biochar primarily occurs through the formation of a uniform monolayer on the adsorbent surface until maximum saturation is achieved [65,66].

The suitability of the Langmuir isotherm model is further supported by the graphical fits for each dye, as shown in Figure 9. The consistency between the kinetic and isothermal models reaffirms that dye adsorption on biochar and activated biochar is predominantly governed by the formation of specific chemical bonds in a monolayer configuration. This alignment provides a comprehensive understanding of the adsorption mechanism and underscores the efficiency of activated biochar as a high-performance adsorbent for the removal of dyes from aqueous solutions.

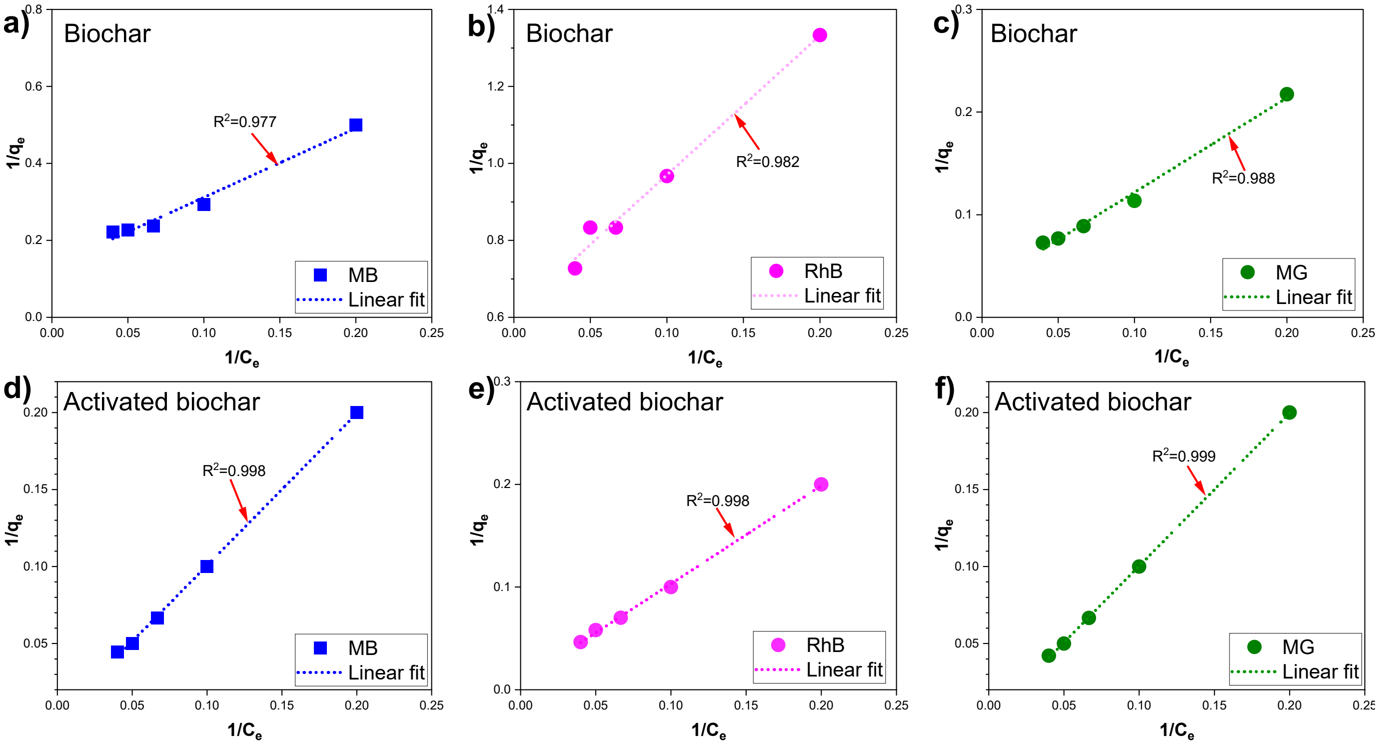

Figure 9. Adsorption Langmuir isotherm study of dye by (**a**–**c**) biochar and (**d**–**f**) activated biochar.

Table 4 presents the Langmuir isotherm parameters, including the maximum adsorption capacity (q_{max}) and the separation factor (R_L), which are critical for assessing the efficiency and selectivity of the adsorption process under the evaluated conditions (10 ppm; pH~7; T = 25 °C). For biochar, the R_L values fall within the range $0 < R_L < 1$, indicating a favorable adsorption process characterized by moderate affinity between the dyes and the biochar [67]. This range suggests that while the biochar efficiently adsorbs the dyes, the interaction is sufficiently weak to permit partial desorption. This aligns with the experimental observations of desorption and readsorption, indicating a reversible and efficient adsorption process.

In contrast, the R_L values for activated biochar are notably low, approaching zero. These values indicate a much stronger interaction between the dyes and the activated material, suggesting high-affinity adsorption nearing irreversibility. This behavior is characteristic of adsorbents with highly reactive and specific surfaces [68]. A comparison of R_L values between biochar and activated biochar reveals a stark difference in both adsorption capacity and the nature of the interactions, underscoring the superior performance of activated biochar. This material is particularly advantageous in applications requiring strong and sustained retention of pollutants.

Table 4. The Langmuir isotherm model results for biochar and activated biochar adsorption.

Materials	Dye	Langmuir Model			
		q_{max} (mg/g)	K_L (L/mg)	R_L (10 ppm)	R^2
Biochar	MB	7.55	13.55	0.0480	0.977
	RhB	1.64	5.95	0.0110	0.982
	MG	33.84	31.20	0.0210	0.988
Activated biochar	MB	470.23	463.86	0.0002	0.998
	RhB	129.53	123.72	0.0008	0.998
	MG	992.72	986.34	0.0001	0.999

Furthermore, q_{max} obtained in this study provides critical insights into the efficiency of the materials for dye removal. For activated biochar, the q_{max} values achieved were 470.23 mg/g for MB, 129.53 mg/g for RhB, and an exceptional 992.72 mg/g for MG. These results demonstrate the remarkable capacity of activated biochar, particularly for MG, where it significantly outperforms other biochar and adsorbents reported in the literature. For instance, water lily-derived biochar [69] and tapioca peel biochar [70] exhibited q_{max} values of 102.35 mg/g and 29.28 mg/g, respectively, for MG, while corn straw-derived biochar [71] reached a higher q_{max} of 515 mg/g. Similarly, for MB, the q_{max} of 470.23 mg/g achieved by the activated biochar significantly exceeds that of biochars derived from lychee seeds (124.5 mg/g) [72] and carbon–silica composites (340.1 mg/g) [73]. Although it falls short of the porous alginate-based hydrogel beads (1426.0 mg/g) [74], activated biochar offers a more cost-effective and scalable alternative with excellent adsorption capacity. For RhB, the q_{max} is 129.53 mg/g, surpassing biochar derived from olive biomass waste (32.81 mg/g) [75] but remaining below the activated carbon derived from jackfruit peel (263.71 mg/g) [76]. These comparisons emphasize the versatility and strong adsorption capacity of the pineapple crown biochar while suggesting that further functionalization could enhance its performance for specific dyes such as RhB.

Overall, the exceptional adsorption capacities achieved by the activated biochar developed in this study highlight its potential as a superior adsorbent for a wide range of dyes, particularly MG. The Langmuir isotherm model provides a reliable framework for understanding and optimizing the adsorption process, reaffirming the suitability of activated biochar as a cost-effective and efficient solution for dye-laden wastewater treatment. Future studies should explore the reusability and long-term performance of this material to fully assess its potential for industrial applications.

4. Conclusions

This study demonstrated that chemical activation of biochar derived from pineapple crown biomass significantly enhances its adsorption capacity for organic dyes, achieving complete removal of MB, RhB, and MG. The superior adsorption performance of the activated biochar, compared to its unmodified counterpart, was attributed to the higher density of active sites generated during the activation process. Kinetic and isotherm analyses revealed that the adsorption process follows a pseudo-second-order model, underscoring the critical role of chemisorption and active site availability in determining process efficiency. The Langmuir isotherm further confirmed that adsorption occurs via monolayer formation on a homogeneous surface, characterized by strong adsorbent–adsorbate affinity. Additionally, activation markedly increased the concentration of oxygenated functional groups (from 13.8% to 49.13%), enhancing surface reactivity and enabling faster adsorption kinetics. Equilibrium was achieved in approximately 9 min for MB and MG under experimental conditions (10 ppm, neutral pH, and ambient temperature). Structural and chemical modifications were validated through SEM, BET, FTIR, and XPS analyses, which revealed significant changes in surface morphology and functionality. These transformations contribute to the high reactivity and exceptional adsorption performance of the material. Compared to other adsorbent materials reported in the literature, activated biochar derived from pineapple crown biomass stands out as a low-cost, efficient, and rapid solution for dye removal in aqueous systems. Although this study primarily focused on initial adsorption efficiency under standard pH and temperature conditions, it is important to consider that factors such as pH, ionic strength, and thermodynamics can significantly influence adsorption performance. Additionally, the reusability of the material after multiple adsorption–regeneration cycles warrants further investigation. Future research should explore the effects of these variables to fully realize the potential of this material as a reusable and scalable adsorbent for industrial and environmental applications. This study highlights its potential as a sustainable solution for water remediation, proposing it as a viable alternative to conventional adsorbents, particularly due to its low cost and abundance of raw materials.

Supplementary Materials: The following supporting information can be downloaded at: https://www.mdpi.com/article/10.3390/su17010099/s1, Table S1: Recent studies on pollutants removal by various biomass-derived biochar; Table S2: Comparison of recent studies on pollutant removal by various biomass−derived biochar; Figure S1: Adsorption Freundlich isotherm of dyes by (a) biochar and (b) activated biochar, [3,69,76–81].

Author Contributions: Conceptualization, O.R.-V. and F.J.C.; methodology, O.R.-V., F.J.C., R.d.P.S.R., S.P.J., M.d.C.H.-C., and R.M.S.-A.; validation, O.R.-V. and F.J.C.; formal analysis, O.R.-V. and F.J.C.; investigation, O.R.-V. and F.J.C.; resources, O.R.-V.; writing—original draft preparation, F.J.C.; writing—review and editing, O.R.-V. and F.J.C.; visualization, H.H.T.-V. and M.G.R.; supervision, A.C.-S. and W.M.-L.; project administration, O.R.-V. All authors have read and agreed to the published version of the manuscript.

Funding: This research received no external funding.

Institutional Review Board Statement: Not applicable.

Informed Consent Statement: Not applicable.

Data Availability Statement: All data included in this study are available upon request by contact with the corresponding author.

Acknowledgments: The authors would like to acknowledge CONAHCYT (Mexico) for the postdoctoral scholarship awarded to Odín Reyes Vallejo (CVU: 487411). The authors thank Rogelio Morán Elvira and María Luisa Ramón García for their technical support with SEM images and XRD research, respectively.

Conflicts of Interest: The authors declare no conflicts of interest.

References

1. Bhattacharya, T.; Khan, A.; Ghosh, T.; Kim, J.T.; Rhim, J.W. Advances and prospects for biochar utilization in food processing and packaging applications. *Sustain. Mater. Technol.* **2024**, *39*, e00831. [CrossRef]
2. Bifulco, A.; Bartoli, M.; Climaco, I.; Franchino, M.C.; Battegazzore, D.; Mensah, R.A.; Das, O.; Vahabi, H.; Malucelli, G.; Aronne, A.; et al. Coffee waste-derived biochar as a flame retardant for epoxy nanocomposites. *Sustain. Mater. Technol.* **2024**, *41*, e01079. [CrossRef]
3. Cano, F.J.; Reyes-Vallejo, O.; Sánchez-Albores, R.M.; Ashok, A.; Vázquez-Vázquez, E.F.; Escobar, S.; Fernández-Madrigal, A.; Sebastian, P.J. Adsorption of Dyes by Charcoal and Activated Charcoal from Moringa Oleifera Leaves. In Proceedings of the 2024 21st International Conference on Electrical Engineering, Computing Science and Automatic Control (CCE), Mexico City, Mexico, 23–25 October 2024; pp. 1–6.
4. Otieno, A.O.; Home, P.G.; Raude, J.M.; Murunga, S.I.; Ngumba, E.; Ojwang, D.O.; Tuhkanen, T. Pineapple peel biochar and lateritic soil as adsorbents for recovery of ammonium nitrogen from human urine. *J. Envion. Manag.* **2021**, *293*, 112794. [CrossRef] [PubMed]

5. Nepal, J.; Ahmad, W.; Munsif, F.; Khan, A.; Zou, Z. Advances and prospects of biochar in improving soil fertility, biochemical quality, and environmental applications. *Front. Environ. Sci.* **2023**, *11*, 1114752. [CrossRef]
6. Luo, L.; Wang, J.; Lv, J.; Liu, Z.; Sun, T.; Yang, Y.; Zhu, Y.G. Carbon Sequestration Strategies in Soil Using Biochar: Advances, Challenges, and Opportunities. *Environ. Sci. Technol.* **2023**, *57*, 11357–11372. [CrossRef]
7. Chiappero, M.; Norouzi, O.; Hu, M.; Demichelis, F.; Berruti, F.; Di Maria, F.; Mašek, O.; Fiore, S. Review of biochar role as additive in anaerobic digestion processes. *Renew. Sustain. Energy Rev.* **2020**, *131*, 110037. [CrossRef]
8. Barquilha, C.E.R.; Braga, M.C.B. Adsorption of organic and inorganic pollutants onto biochars: Challenges, operating conditions, and mechanisms. *Bioresour. Technol. Rep.* **2021**, *15*, 100728. [CrossRef]
9. Dai, L.; Lu, Q.; Zhou, H.; Shen, F.; Liu, Z.; Zhu, W.; Huang, H. Tuning oxygenated functional groups on biochar for water pollution control: A critical review. *J. Hazard. Mater.* **2021**, *420*, 126547. [CrossRef] [PubMed]
10. Tan, X.F.; Zhu, S.S.; Wang, R.P.; Chen, Y.D.; Show, P.L.; Zhang, F.F.; Ho, S.H. Role of biochar surface characteristics in the adsorption of aromatic compounds: Pore structure and functional groups. *Chin. Chem. Lett.* **2021**, *32*, 2939–2946. [CrossRef]
11. Xie, Y.; Wang, L.; Li, H.; Westholm, L.J.; Carvalho, L.; Thorin, E.; Yu, Z.; Yu, X.; Skreiberg, Ø. A critical review on production, modification and utilization of biochar. *J. Anal. Appl. Pyrolysis* **2022**, *161*, 105405. [CrossRef]
12. Panwar, N.L.; Pawar, A. Influence of activation conditions on the physicochemical properties of activated biochar: A review. *Biomass Convers. Biorefin.* **2022**, *12*, 925–947. [CrossRef]
13. Hsiao, C.H.; Gupta, S.; Lee, C.Y.; Tai, N.H. Effects of physical and chemical activations on the performance of biochar applied in supercapacitors. *Appl. Surf. Sci.* **2023**, *610*, 155560. [CrossRef]
14. Gęca, M.; Wiśniewska, M.; Nowicki, P. Biochars and activated carbons as adsorbents of inorganic and organic compounds from multicomponent systems—A review. *Adv. Colloid. Interface Sci.* **2022**, *305*, 102687. [CrossRef]
15. Zhang, Z.; Wang, T.; Zhang, H.; Liu, Y.; Xing, B. Adsorption of Pb(II) and Cd(II) by magnetic activated carbon and its mechanism. *Sci. Total Environ.* **2021**, *757*, 143910. [CrossRef] [PubMed]
16. Goswami, L.; Kushwaha, A.; Kafle, S.R.; Kim, B.-S. Surface Modification of Biochar for Dye Removal from Wastewater. *Catalysts* **2022**, *12*, 817. [CrossRef]
17. Anegbe, B.; Ifijen, I.H.; Maliki, M.; Uwidia, I.E.; Aigbodion, A.I. Graphene oxide synthesis and applications in emerging contaminant removal: A comprehensive review. *Environ. Sci. Eur.* **2024**, *36*, 1–34. [CrossRef]
18. Díaz, B.; Sommer-Márquez, A.; Ordoñez, P.E.; Bastardo-González, E.; Ricaurte, M.; Navas-Cárdenas, C. Synthesis Methods, Properties, and Modifications of Biochar-Based Materials for Wastewater Treatment: A Review. *Resources* **2024**, *13*, 8. [CrossRef]
19. Assaf, K.I.; Nau, W.M. Dispersion Interactions in Condensed Phases and inside Molecular Containers. *Acc. Chem. Res.* **2023**, *56*, 3451–3461. [CrossRef] [PubMed]
20. Rojas-Chávez, H.; Miralrio, A.; Hernández-Rodríguez, Y.M.; Cruz-Martínez, H.; Pérez-Pérez, R.; Cigarroa-Mayorga, O.E. Needle- and cross-linked ZnO microstructures and their photocatalytic activity using experimental and DFT approach. *Mater. Lett.* **2021**, *291*, 129474. [CrossRef]
21. Ikram, M.; Rashid, M.; Haider, A.; Naz, S.; Haider, J.; Raza, A.; Ansar, M.T.; Uddin, M.K.; Ali, N.M.; Ahmed, S.S.; et al. A review of photocatalytic characterization, and environmental cleaning, of metal oxide nanostructured materials. *Sustain. Mater. Technol.* **2021**, *30*, e00343. [CrossRef]
22. Reyes-Vallejo, O.; Sánchez-Albores, R.; Ashok, A.; Serrano-Ramirez, R.P.; Durán-Álvarez, J.C.; Bartolo-Pérez, P.; Cano, F.J.; Velumani, S. $BiVO_4$ synthesized by the combustion method: A comparison between orange peel powder and urea used as fuel. *J. Mater. Sci. Mater. Electron.* **2024**, *35*, 1245. [CrossRef]
23. Reyes-Vallejo, O.; Sánchez-Albores, R.M.; Adhikari, A. Graphene-Based Materials and Metal Oxide Composites for Photocatalytic Degradation of Pollutants. In *Graphene-Based Photocatalysts: From Fundamentals to Applications*; Springer Nature: Cham, Switzerland, 2024; pp. 667–696. [CrossRef]
24. Rangel-Contreras, V.; Reyes-Vallejo, O.; Subramaniam, V. Synthesis of TiO_2/CuO/GO nanocomposite for the photocatalytic degradation of methylene blue. *J. Mater. Sci. Mater. Electron.* **2024**, *35*, 1301. [CrossRef]
25. Adhikari, A.; Sánchez-Albores, R.M.; Reyes-Vallejo, O. A Perspective on the Graphene-Based Materials Toward Eco-friendly Synthesis Methods. In *Graphene-Based Photocatalysts: From Fundamentals to Applications*; Springer Nature: Cham, Switzerland, 2024; pp. 89–100. [CrossRef]
26. Cano, F.J. Influence of Graphene Oxide (GO) on TiO_2-GO Nanostructures Applied to Water Pollution Control. Available online: https://inria.hal.science/tel-04733514/ (accessed on 15 November 2024).
27. Amato, F.; Motta, A.; Giaccari, L.; Di Pasquale, R.; Scaramuzzo, F.A.; Zanoni, R.; Marrani, A.G. One-pot carboxyl enrichment fosters water-dispersibility of reduced graphene oxide: A combined experimental and theoretical assessment. *Nanoscale Adv.* **2023**, *5*, 893–906. [CrossRef] [PubMed]
28. Peng, W.; Hu, Y.; Wang, C.; Li, H.; Liu, Y.; Song, S. Enhanced adsorption performance of the graphene oxide with metallic ion impurities by elution. *Surf. Interface Anal.* **2017**, *49*, 728–734. [CrossRef]

29. Panich, A.M.; Shames, A.I.; Sergeev, N.A. Paramagnetic Impurities in Graphene Oxide. *Appl. Magn. Reson.* **2013**, *44*, 107–116. [CrossRef]
30. Ali, L.; Palamanit, A.; Techato, K.; Ullah, A.; Chowdhury, M.S.; Phoungthong, K. Characteristics of Biochars Derived from the Pyrolysis and Co-Pyrolysis of Rubberwood Sawdust and Sewage Sludge for Further Applications. *Sustainability* **2022**, *14*, 3829. [CrossRef]
31. Wardhono, E.Y.; Pinem, M.P.; Susilo, S.; Siom, B.J.; Sudrajad, A.; Pramono, A.; Meliana, Y.; Guénin, E. Modification of Physio-Mechanical Properties of Chitosan-Based Films via Physical Treatment Approach. *Polymers* **2022**, *14*, 5216. [CrossRef] [PubMed]
32. Bohari, N.; Mohidin, H.; Idris, J.; Andou, Y.; Man, S.; Saidan, H.; Mahdian, S. Nutritional characteristics of biochar from pineapple leaf residue and sago waste. *Pertanika J. Sci. Technol.* **2020**, *28*, 273–286. [CrossRef]
33. Nayan, M.B.; Jagadish, K.; Abhilash, M.R.; Namratha, K.; Srikantaswamy, S. Comparative Study on the Effects of Surface Area, Conduction Band and Valence Band Positions on the Photocatalytic Activity of ZnO-M_xO_y Heterostructures. *J. Water Resour. Prot.* **2019**, *11*, 357–370. [CrossRef]
34. Starsinic, M.; Taylor, R.L.; Walker, P.L.; Painter, P.C. FTIR studies of Saran chars. *Carbon N. Y.* **1983**, *21*, 69–74. [CrossRef]
35. Giannakopoulos, S.; Vakros, J.; Frontistis, Z.; Manariotis, I.D.; Venieri, D.; Poulopoulos, S.G.; Mantzavinos, D. Biochar from Lemon Stalks: A Highly Active and Selective Carbocatalyst for the Oxidation of Sulfamethoxazole with Persulfate. *Catalysts* **2023**, *13*, 233. [CrossRef]
36. Cano, F.J.; Reyes-Vallejo, O.; Ashok, A.; Olvera, M.D.L.L.; Velumani, S.; Kassiba, A. Mechanisms of dyes adsorption on titanium oxide–graphene oxide nanocomposites. *Ceram. Int.* **2023**, *49*, 21185–21205. [CrossRef]
37. Andrade, T.S.; Vakros, J.; Mantzavinos, D.; Lianos, P. Biochar obtained by carbonization of spent coffee grounds and its application in the construction of an energy storage device. *Chem. Eng. J. Adv.* **2020**, *4*, 100061. [CrossRef]
38. Popova, A.N. Crystallographic analysis of graphite by X-Ray diffraction. *Coke Chem.* **2017**, *60*, 361–365. [CrossRef]
39. Cano, F.J.; Romero-Núñez, A.; Liu, H.; Reyes-Vallejo, O.; Ashok, A.; Velumani, S.; Kassiba, A. Variation in the bandgap by gradual reduction of GOs with different oxidation degrees: A DFT analysis. *Diam. Relat. Mater.* **2023**, *139*, 110382. [CrossRef]
40. Peng, H.; Li, K.; Wang, T.; Wang, J.; Wang, J.; Zhu, R.; Sun, D.; Wang, S. Preparation of hierarchical mesoporous $CaCO_3$ by a facile binary solvent approach as anticancer drug carrier for etoposide. *Nanoscale Res. Lett.* **2013**, *8*, 321. [CrossRef] [PubMed]
41. Luo, Q.; Deng, Y.; Li, Y.; He, Q.; Wu, H.; Fang, X. Effects of pyrolysis temperatures on the structural properties of straw biochar and its adsorption of tris-(1-chloro-2-propyl) phosphate. *Sci. Rep.* **2024**, *14*, 25711. [CrossRef]
42. Arregui-Mena, J.D.; Worth, R.N.; Bodel, W.; März, B.; Li, W.; Selby, A.; Campbell, A.A.; Contescu, C.; Edmondson, P.D.; Gallego, N. SEM and TEM data of nuclear graphite and glassy carbon microstructures. *Data Brief.* **2023**, *46*, 108808. [CrossRef] [PubMed]
43. Cano, F.J.; Coste, S.; Reyes-Vallejo, O.; Makowska-Janusik, M.; Velumani, S.; Olvera, M.d.l.L.; Kassiba, A. Influence of GO oxidation degrees on the organization and physical features of TiO_2–GO-based nanocomposites for water dye removal. *Surf. Interfaces* **2024**, *46*, 104004. [CrossRef]
44. de Almeida, S.G.C.; Tarelho, L.A.C.; Hauschild, T.; Costa, M.A.M.; Dussán, K.J. Biochar production from sugarcane biomass using slow pyrolysis: Characterization of the solid fraction. *Chem. Eng. Process. —Process Intensif.* **2022**, *179*, 109054. [CrossRef]
45. Yu, J.; Ding, H.; Zhang, Z.L.; Li, Y.; Ding, L. Sorption characteristics and mechanism of oxytetracycline in water by modified biochar derived from chestnut shell. *Zhongguo Huanjing Kexue/China Environ. Sci.* **2021**, *41*, 5688–5700.
46. Pareek, S.; Jain, D.; Shrivastava, R.; Dam, S.; Hussain, S.; Behera, D. Tunable degree of oxidation in graphene oxide: Cost effective synthesis, characterization and process optimization. *Mater. Res. Express.* **2019**, *6*, 085625. [CrossRef]
47. Zhou, S.; Bongiorno, A. Origin of the Chemical and Kinetic Stability of Graphene Oxide. *Sci. Rep.* **2013**, *3*, 2484. [CrossRef]
48. Hoffmann, G.; Rathinam, K.; Martschin, M.; Ivančev-Tumbas, I.; Panglisch, S. Influence of carbon agglomerate formation on micropollutants removal in combined PAC-membrane filtration processes for advanced wastewater treatment. *Water* **2021**, *13*, 3578. [CrossRef]
49. Huang, N.; Chen, X.; Krishna, R.; Jiang, D. Two-dimensional covalent organic frameworks for carbon dioxide capture through channel-wall functionalization. *Angew. Chem. Int. Ed.* **2015**, *54*, 2986–2990. [CrossRef] [PubMed]
50. Lafi, R.; Montasser, I.; Hafiane, A. Adsorption of congo red dye from aqueous solutions by prepared activated carbon with oxygen-containing functional groups and its regeneration. *Adsorpt. Sci. Technol.* **2019**, *37*, 160–181. [CrossRef]
51. Yin, G.; Sun, Z.; Gao, Y.; Xu, S. Preparation of expanded graphite for malachite green dye removal from aqueous solution. *Microchem. J.* **2021**, *166*, 106190. [CrossRef]
52. Cao, S.; Zhu, R.; Wu, D.; Su, H.; Liu, Z.; Chen, Z. How hydrogen bonding and π–π interactions synergistically facilitate mephedrone adsorption by bio-sorbent: An in-depth microscopic scale interpretation. *Environ. Pollut.* **2024**, *342*, 123044. [CrossRef]
53. Thakuria, R.; Nath, N.K.; Saha, B.K. The Nature and Applications of π-π Interactions: A Perspective. *Cryst. Growth Des.* **2019**, *19*, 523–528. [CrossRef]
54. Maier, P.; Xavier, N.F.; Truscott, C.L.; Hansen, T.; Fouquet, P.; Sacchi, M.; Tamtögl, A. How does tuning the van der Waals bonding strength affect adsorbate structure? *Phys. Chem. Chem. Phys.* **2022**, *24*, 29371–29380. [CrossRef]

55. Adeyi, A.A.; Jamil, S.N.A.M.; Abdullah, L.C.; Choong, T.S.Y.; Lau, K.L.; Alias, N.H. Simultaneous adsorption of malachite green and methylene blue dyes in a fixed-bed column using poly (acrylonitrile-co-acrylic acid) modified with thiourea. *Molecules* **2020**, *25*, 2650. [CrossRef] [PubMed]
56. Melhi, S.; Alqadami, A.A.; Alosaimi, E.H.; Ibrahim, G.M.; El-Gammal, B.; Bedair, M.A.; Elnaggar, E.M. Effective Removal of Malachite Green Dye from Water Using Low-Cost Porous Organic Polymers: Adsorption Kinetics, Isotherms, and Reusability Studies. *Water* **2024**, *16*, 1869. [CrossRef]
57. Kuśmierek, K.; Fronczyk, J.; Świątkowski, A. Adsorptive Removal of Rhodamine B Dye from Aqueous Solutions Using Mineral Materials as Low-Cost Adsorbents. *Water Air Soil. Pollut.* **2023**, *234*, 531. [CrossRef]
58. Lesniewicz, A.; Lewandowska-Andralojc, A. Probing mechanism of Rhodamine B decolorization under homogeneous conditions via pH-controlled photocatalysis with anionic porphyrin. *Sci. Rep.* **2024**, *14*, 22600. [CrossRef] [PubMed]
59. Ederer, J.; Ecorchard, P.; Slušná, M.Š.; Tolasz, J.; Smržová, D.; Lupínková, S.; Janoš, P. A Study of Methylene Blue Dye Interaction and Adsorption by Monolayer Graphene Oxide. *Adsorpt. Sci. Technol.* **2022**, *2022*, 7385541. [CrossRef]
60. Ouachtak, H.; El Haouti, R.; El Guerdaoui, A.; Haounati, R.; Amaterz, E.; Addi, A.A.; Akbal, F.; Taha, M.L. Experimental and molecular dynamics simulation study on the adsorption of Rhodamine B dye on magnetic montmorillonite composite γ-Fe_2O_3@Mt. *J. Mol. Liq.* **2020**, *309*, 113142. [CrossRef]
61. dos Reis, G.S.; Bergna, D.; Grimm, A.; Lima, E.C.; Hu, T.; Naushad, M.; Lassi, U. Preparation of highly porous nitrogen-doped biochar derived from birch tree wastes with superior dye removal performance. *Colloids Surf. A Physicochem. Eng. Asp.* **2023**, *669*, 131493. [CrossRef]
62. Wu, F.C.; Tseng, R.L.; Juang, R.S. Initial behavior of intraparticle diffusion model used in the description of adsorption kinetics. *Chem. Eng. J.* **2009**, *153*, 1–8. [CrossRef]
63. Tran, H.N.; You, S.J.; Hosseini-Bandegharaei, A.; Chao, H.P. Mistakes and inconsistencies regarding adsorption of contaminants from aqueous solutions: A critical review. *Water Res.* **2017**, *120*, 88–116. [CrossRef] [PubMed]
64. Pan, Y.; Shi, X.; Cai, P.; Guo, T.; Tong, Z.; Xiao, H. Dye removal from single and binary systems using gel-like bioadsorbent based on functional-modified cellulose. *Cellulose* **2018**, *25*, 2559–2575. [CrossRef]
65. Wei, H.; Zhao, J.J.; Jing, L.M.; Niu, J.F.; Fu, R.; Dong, W. Adsorption of Iopamidol by $NaHCO_3$-activated Buckwheat Biochar. *Huanjing Kexue/Environ. Sci.* **2023**, *44*, 6811–6822. [CrossRef]
66. Kalam, S.; Abu-Khamsin, S.A.; Kamal, M.S.; Patil, S. Surfactant Adsorption Isotherms: A Review. *ACS Omega* **2021**, *6*, 32342–32348. [CrossRef] [PubMed]
67. Garbovskiy, Y. A perspective on the Langmuir adsorption model applied to molecular liquid crystals containing ions and nanoparticles. *Front. Soft Matter.* **2022**, *2*, 1079063. [CrossRef]
68. Shamohammadi, S.; Aghabozorgi, N.; Motaghian, H.R.; Semnani, A. Introducing the law of "irreversibility" in the dynamic equilibrium of mass. *Case Stud. Chem. Environ. Eng.* **2024**, *10*, 100746. [CrossRef]
69. Jabar, J.M.; Odusote, Y.A. Utilization of prepared activated biochar from water lily (Nymphaea lotus) stem for adsorption of malachite green dye from aqueous solution. *Biomass Convers. Biorefin.* **2024**, *14*, 5999–6010. [CrossRef]
70. Vigneshwaran, S.; Sirajudheen, P.; Karthikeyan, P.; Meenakshi, S. Fabrication of sulfur-doped biochar derived from tapioca peel waste with superior adsorption performance for the removal of Malachite green and Rhodamine B dyes. *Surf. Interfaces* **2021**, *23*, 100920. [CrossRef]
71. Eltaweil, A.S.; Ali Mohamed, H.; Abd El-Monaem, E.M.; El-Subruiti, G.M. Mesoporous magnetic biochar composite for enhanced adsorption of malachite green dye: Characterization, adsorption kinetics, thermodynamics and isotherms. *Adv. Powder Technol.* **2020**, *31*, 1253–1263. [CrossRef]
72. Sahu, S.; Pahi, S.; Tripathy, S.; Singh, S.K.; Behera, A.; Sahu, U.K.; Patel, R.K. Adsorption of methylene blue on chemically modified lychee seed biochar: Dynamic, equilibrium, and thermodynamic study. *J. Mol. Liq.* **2020**, *315*, 113743. [CrossRef]
73. Lv, J.L.; Zhai, S.R.; Wang, Z.Z.; Lei, Z.M.; An, Q. Da: Carbon-silica composite bio-sorbents with a high density of oxygen-containing sites for efficient methylene blue adsorption. *Res. Chem. Intermed.* **2016**, *42*, 839–854. [CrossRef]
74. Pei, Y.-Y.; Guo, D.-M.; An, Q.-D.; Xiao, Z.-Y.; Zhai, S.-R.; Zhai, B. Hydrogels with diffusion-facilitated porous network for improved adsorption performance. *Korean J. Chem. Eng.* **2018**, *35*, 2384–2393. [CrossRef]
75. Albanio, I.I.; Muraro, P.C.L.; da Silva, W.L. Rhodamine B Dye Adsorption onto Biochar from Olive Biomass Waste. *Water Air Soil. Pollut.* **2021**, *232*, 214. [CrossRef]
76. Yusop, M.F.M.; Abdullah, A.Z.; Ahmad, M.A. Adsorption of remazol brilliant blue R dye onto jackfruit peel based activated carbon: Optimization and simulation for mass transfer and surface area prediction. *Inorg. Chem. Commun.* **2023**, *158*, 111721. [CrossRef]
77. Ahmad, M.A.; Alrozi, R. Removal of malachite green dye from aqueous solution using rambutan peel-based activated carbon: Equilibrium, kinetic and thermodynamic studies. *Chem. Eng. J.* **2011**, *171*, 510–516. [CrossRef]
78. Mahmud, K.N.; Wen, T.H.; Zakaria, Z.A. Activated carbon and biochar from pineapple waste biomass for the removal of methylene blue. *Environ. Toxicol. Manag.* **2021**, *1*, 30–36. [CrossRef]

79. Gao, G.L.; Zhou, P.J. Green synthesis of functional biochar derived from sediment/blue algae/rectorite and the enhanced interaction of DNA in the aquatic environments: A mechanistic study. *Biomass Conv. Bioref.* **2023**. [CrossRef]
80. Sutradhar, S.; Mondal, A.; Kuehne, F.; Krueger, O.; Rakshit, S.K.; Kang, K. Comparison of Oil-Seed Shell Biomass-Based Biochar for the Removal of Anionic Dyes—Characterization and Adsorption Efficiency Studies. *Plants* **2024**, *13*, 820. [CrossRef]
81. Yagub, M.T.; Sen, T.K.; Afroze, S.; Ang, H.M. Dye and its removal from aqueous solution by adsorption: A review. *Adv. Colloid Interface Sci.* **2014**, *209*, 172–184. [CrossRef] [PubMed]